

# Formation of glacier tables caused by differential ice melting: field observation and modelling

Marceau Hénot<sup>1</sup>, Vincent J. Langlois<sup>2</sup>, Nicolas Plihon<sup>1</sup>, and Nicolas Taberlet<sup>1</sup>

<sup>1</sup>Univ Lyon, Ens de Lyon, Univ Claude Bernard, CNRS, Laboratoire de Physique, F-69342 Lyon, France

<sup>2</sup>Laboratoire de Géologie de Lyon, Terre, Planètes, Environnement, Université Claude Bernard Lyon 1 - ENS de Lyon - Université Jean Monnet Saint-Étienne - CNRS, France

**Correspondence:** Nicolas Taberlet <nicolas.taberlet@ens-lyon.fr>

## Abstract.

Glacier tables are structures frequently encountered on temperate glaciers. They consist of a rock supported by a narrow ice foot which forms through differential melting of the ice. In this article, we investigate their formation by following their dynamics on the Mer de Glace (Alps, France). We report field measurements of four specific glacier tables over the course of several days, as well as snapshot measurements of a field of 80 tables performed on one given day. We develop a simple model accounting for the various mechanisms of the heat transfer on the glacier using local meteorological data, which displays a quantitative agreement with the field measurements. We show that the formation of glacier tables is controlled by the global heat flux received by the rocks which causes the ice underneath to melt. Under large rocks the ice ablation rate is reduced compared to bare ice leading to the formation of glacier tables. Under a critical size however, which depends on the meteorological conditions, rocks can enhance ice melting and consequently sink into the ice surface.

## 1 Introduction

A wide variety of spectacular shapes and patterns formed through differential ablation can be found in Nature: surface patterns known as rillenkarren result from the dissolution of soluble rocks (Cohen et al., 2016; Claudin et al., 2017; Cohen et al., 2020; Guérin et al., 2020), tafoni are cavernous rock domes dug by salt crystallization during wetting/drying cycles (Huinink et al., 2004), scallops and sharp pinnacles are created by convective flows (Huang et al., 2020; Weady et al., 2022), mushroom rocks undergo erosion of their base by strong particle-laden winds (Mashaal et al., 2020), and hoodoos which consist of a hard stone protecting a narrow column of sedimentary rock from rain-induced erosion (Young and Young, 1992; Bruthans et al., 2014; Turkington and Paradise, 2005).

On ice and snow surfaces, similar structures can be found: slender snow blades known as penitentes (Mangold, 2011; Bergeron et al., 2006; Claudin et al., 2015), as well as blue ice ripples observed in Antarctica (Bintanja et al., 2001) and on Mars (Bordiec et al., 2020) are caused by sublimation, suncusps are bowl-shaped depressions found at the surface of a snow patch (Rhodes et al., 1987; Betterton, 2001; Mitchell and Tiedje, 2010), scallops are regularly spaced patterns of surface indentations at the ice-water or ice-air interface (Bushuk et al., 2019), ice sails (or pyramids) are larger bare ice structures forming on debris covered glaciers (Evatt et al., 2017; Fowler and Mayer, 2017), Zen stones found on frozen lakes are pebbles

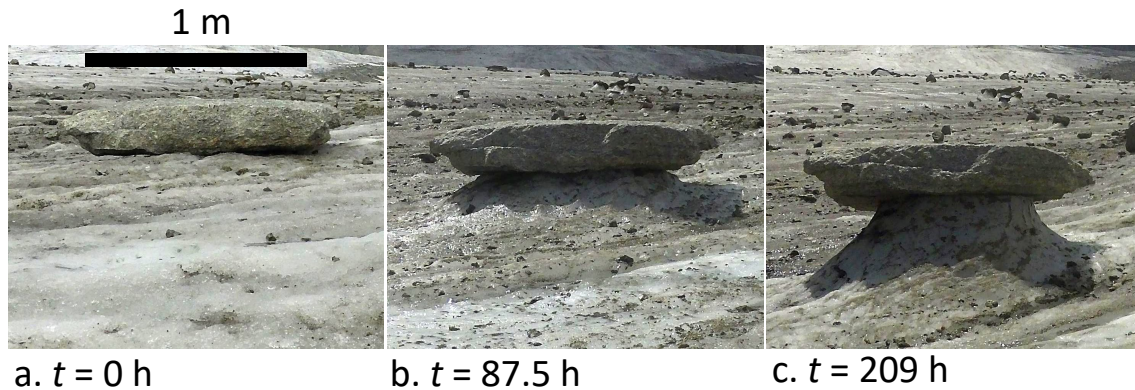


**Figure 1.** (a, b, c) Formation of a natural granite glacier table (rock 1, see Table 1).

25 resting on a delicate ice pedestal protected from sun-induced sublimation (Taberlet and Plihon, 2021) and glacier tables (see  
 fig. 1c) for which a foot of ice resists melting due mostly to thermal insulation provided by a large rock (Agassiz, 1840;  
 Bouillette, 1933, 1934; Smiraglia and Diolaiuti, 2011; Hénot et al., 2021).

On a temperate glacier, the ice ablation rate is influenced by the presence of debris on its surface. Indeed, a dense debris  
 layer covering an ice surface can, when thin enough (less than 0.5 cm), enhance the ice melting compared to a bare ice surface  
 30 or, if thick enough, act as an insulation layer and reduce the melting rate (Östrem, 1959). The insulation effect is well-captured  
 by complex energy balance models which use meteorological data as input parameters (Reid and Brock, 2010; Collier et al.,  
 2014), and more recently using enhanced temperature index models (Carenzo et al., 2016; Moeller et al., 2016). The melt  
 amplification effect for thin debris layers was explained by its patchiness (Reid and Brock, 2010) or by its porosity to air  
 flow (Evatt et al., 2015). At a more local scale, patches of dirt or ashes on a glacier are known to lead to the formation of  
 35 ice structures known as dirt cones, which consists of an ice cone covered with a centimetric layer of dirt (Swithinbank, 1950;  
 Krenek, 1958; Drewry, 1972; Betterton, 2001).

Glacier tables (see fig. 1c) are structures frequently encountered on the leveled part of temperate glaciers (Agassiz, 1840).  
 They typically consist of a meter-size rock supported by a column (or foot) of ice. They form over the course of a few days to  
 a few weeks at the end of the spring, from May to June and may progressively disappear during the summer. Very large tables  
 40 however, whose size can reach 10 m, can last for several years (Bouillette, 1933, 1934). Glacier tables form because the ablation  
 rate of the ice is lower under the rock than at the air-ice interface. When the ice foot becomes too thin, the table falls, usually  
 on its south side. The ice foot progressively disappears and the rock can potentially form another table, if not too late in the  
 season. Similarly to what is know for debris layers, smaller rocks tend not to form tables but can instead increase the melting  
 rate and gradually sink into the ice, creating narrow and deep holes which can reach up to 15 cm in depth (McIntyre, 1984). In  
 45 a previous work (Hénot et al., 2021), artificial glacier tables were reproduced experimentally in a lab controlled environment  
 (constant temperature, humidity, absence of wind), at a centimetric scale. The study focused on the initial behavior of pattern  
 formation using cylindrical "rocks" of various sizes, aspect ratio and materials, initially resting on a flat ice surface. Although

this small scale study under controlled conditions allowed one to understand the physical mechanisms that could play a role in glacier table formation, it did not encompass the complexity of the energy balance on a natural glacier, in particular the effects of the direct solar irradiation and of the wind.

In this article, we report field observations made on the Mer de Glace (French Alps) of the formation dynamics of glacier tables monitored over the course of a few days, as well as a systematic measurement of already-formed tables on a given day. The Mer de Glace is a temperate glacier, meaning that the ice temperature is always given by the melting temperature of water,  $T_{\text{ice}} = 273$  K. We use local meteorological data to fit the ice ablation rate and characterize the heat transfer mechanisms at the surface of the glacier. We then develop a 1D conduction model taking into account the effect of the solar irradiation as well as sensible and longwave heat fluxes, which is in excellent agreement with the field measurements and which illustrates the synergistic effect between solar irradiation and sensible flux responsible for glacier table formation.

## 2 Observation

### 2.1 Location and definitions

In this article, we report two sets of observations made on the Mer de Glace: a time-resolved camera recording of the formation and evolution of four glacier tables and a field observation of 80 glacier tables.

The lower part of the Mer de Glace (below a 2100 m altitude) is largely covered with granitic debris, with sizes ranging from submillimetric up to several meters. In the following, their dimensions are characterized by their thickness  $h$  and their larger and smaller widths  $d_1$  and  $d_2$  (see fig. 2b). We define an effective width of the rock  $d_{\text{eff}} = 2d_1d_2/(d_1 + d_2)$  whose expression will be justified in part 3.2 and the aspect ratio  $\beta = h/d_{\text{eff}}$ . The vertical distance from the bottom of a rock to the surface of the ice far from it is denoted  $H$ . This quantity is either positive if the rock forms a table, in which case it corresponds to the height of the ice foot, or negative if the rock sinks into the ice surface, in which case it correspond to the depth of the hole.

### 2.2 Time evolution of four large tables

Time-lapse images were obtained using an autonomous solar powered camera (Enlaps Tikee) placed on three 1.5 m-long wood rods set into the ice. Pictures (4608 px  $\times$  3456 px) were taken every 30 min between 5 am and 10 pm during 5 to 7 days until the camera fell on the ice due to the melting around the supporting rods. The movements of the device were corrected by tracking two fixed points on the background of the images. The positions of the top of the rocks were then manually pointed on each image. The formation of glacier tables created by four granite rocks of various shapes and dimensions was recorded in two time periods: A (7-14 June 2019) and B (4-9 June 2021), situated respectively on location 3 and 2 on the map of fig. 2a, as summarized in table 1. Rocks 1, 2 and 4 were moved on clean flat ice, in front of the camera, the day before the recording started in order to provide a controlled initial state in which the rocks are lying on a horizontal ice surface ( $H = 0$ , see fig. 1a). Rock 3 was already standing on an ice foot, approximately 1 m high, at the beginning of period B (see the supplementary

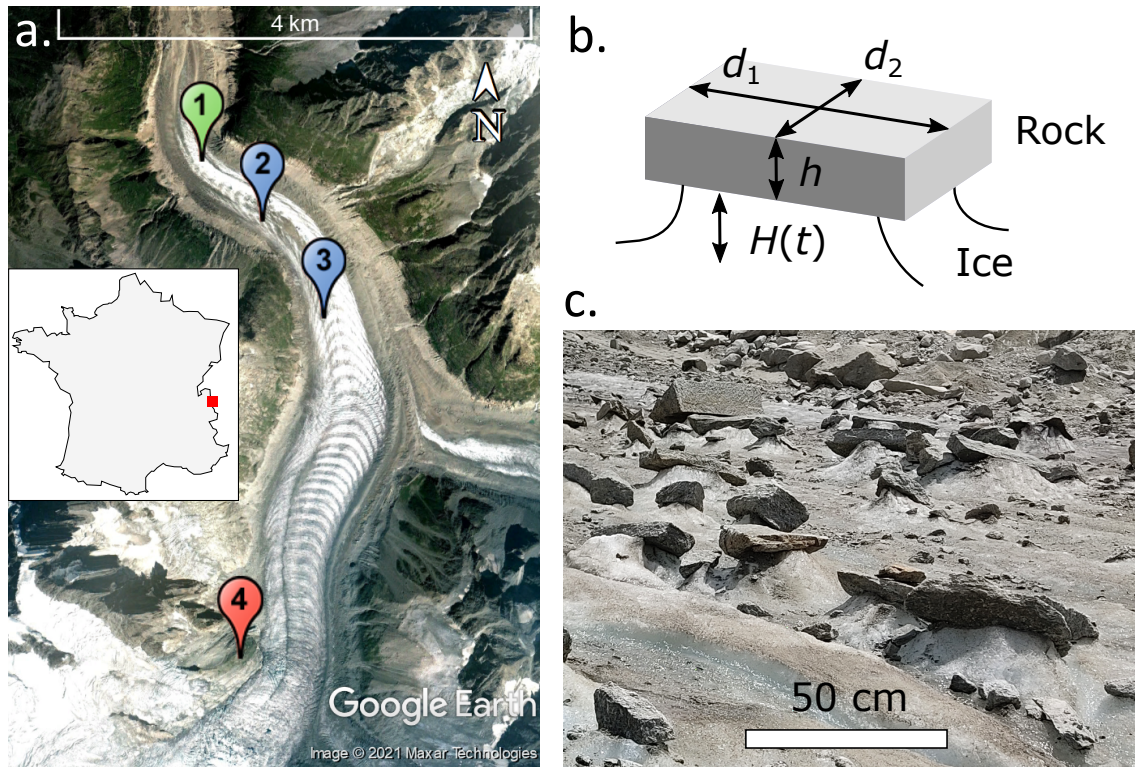


**Figure 2.** (a) Map of the Mer de Glace in the French Alps (Google Earth Image © 2021 Maxar Technologies) locating the measurement site of June 3<sup>rd</sup> 2021 (1), the timelapse observation sites of June 2021 (2) and June 2019 (3) and the Requin AWS (4). (b) 3D schematics of a typical glacier table defining the height  $H(t)$  of the ice foot and the average thickness  $h$  and widths  $d_1$  and  $d_2$  of the rock. (c) Picture of a portion of the glacier taken in June 2021 showing natural glacier tables, from which the data shown in fig. 3 were obtained.

material). The evolution of the vertical position of these rocks is plotted in fig. 4a and b. The position of the ice surface was followed using a scaling rod, embedded into the ice and located approximately 2 m away from the rocks.

80 The surface temperature of rock 4 was measured every 5 min during period B using thermocouples and a homemade battery powered device (Arduino MKR ZERO and EVAL-CN0391-ARDZ Shield). The wind speed  $u_a$ , air temperature  $T_a$ , air specific humidity  $q_a$  and solar radiative flux  $\Phi$  were measured at the Requin automatic weather station (AWS) (see Nadeau et al. (2009), that uses identical devices for a detailed description), at  $z_m = 5$  m above ground (located at 45.8846°N, 06.9297°E, see marker 4 on fig. 2a), 600 m higher and 3 km away from the measurement site. The time resolution was 1 h in 2019 and 15 min in 2021. On a 2-week time period in July 2021, we also measured the air temperature at location 2, 3 m above the glacier surface (see the supplementary material) which was systematically 2.5°C higher than the AWS data. In the rest of the article, we use the AWS data to which an offset was added:  $T_a = T_{a\_AWS} + 2.5^\circ\text{C}$ . We do not expect the measured solar flux and the wind speed to be significantly affected by the distance from the measurement site. The incoming longwave radiation coming from the atmosphere  $Q_{LW\ atm\ \downarrow}$  was obtained from the S2M (SAFRAN - SURFEX/ISBA-Crocus - MEPRA)

**Table 1.** Characteristics of the rocks studied.

Rock index	Location	Altitude	GPS coord.	Period of observation	$h$ (m)	$d_1/d_2$ (m)	$\beta$
1	3	2020 m	45.9095°N	A:	0.25	1.21 / 0.98	0.23
2			06.9384°E	7-14 Jun. 19	0.12	0.41 / 0.35	0.32
3	2	1910 m	45.9168°N	B:	1.7	3.5 / 3.5	0.49
4			06.9319°E	4-9 Jun. 21	0.095	0.32/0.31	0.30

90 reanalysis, which combine information from numerical weather prediction models and in-situ meteorological observation to estimate massif-averaged meteorological data with a 1 h time resolution (Vernay et al., 2021) (the parameters used to compute the meteorological data in this study are the closest available representative of the real field, i.e. massif 3, 2100 m altitude, 20° slope facing north). The meteorological data are displayed in fig. 4c-l.

### 2.3 An 800-m<sup>2</sup> field comprising 80 glacier tables

95 On June 3<sup>rd</sup> 2021, we systematically measured, in an area of 10 m×80 m located at point 1 in fig. 2a, the dimensions of granite rocks (thickness and widths) as well as either the height of the ice foot supporting them ( $H > 0$ ) or the depth of penetration in the ice ( $H < 0$ ). The data of  $H$  is plotted in fig. 3 as a function of the thickness  $h$  and the widths  $d_1$  and  $d_2$  of the rocks.

## 3 Model

### 3.1 Energy balance at the ice surface

100 In the following, we characterize the heat flux balance on the glacier surface by linking the ablated ice thickness to local meteorological data in the same way it was done previously in the literature (Hock, 2005; Conway and Cullen, 2013; Fitzpatrick et al., 2017). The net incident heat flux causing the glacier surface to melt with an open environment can be expressed as:

$$Q_{\text{open env.} \rightarrow \text{ice}} = Q_{\text{SW}}^i + Q_{\text{LW}}^i + Q_{\text{H}}^i + Q_{\text{L}}^i + Q_{\text{R}}^i \quad (1)$$

where  $Q_{\text{SW}}^i$  and  $Q_{\text{LW}}^i$  are the net shortwave and longwave radiative fluxes,  $Q_{\text{H}}^i$  and  $Q_{\text{L}}^i$  are the turbulent heat fluxes corresponding respectively to sensible and latent heat and  $Q_{\text{R}}^i$  is the flux associated with rain. The shortwave radiation (when neglecting the reflected radiation by the surrounding terrain) is given by  $Q_{\text{SW}}^i = \Phi(1 - \alpha_{\text{ice}})$ , where  $\alpha_{\text{ice}}$  is the ice albedo and  $\Phi$  is the incoming solar radiative flux (direct and diffuse) given by the meteorological S2M reanalysis model. The net longwave flux comes from a balance between the radiation received by the ice from the atmosphere  $Q_{\text{LW atm } \downarrow}^i$  and the radiation emitted by the ice  $Q_{\text{LW } \uparrow}^i$  at temperature  $T_{\text{ice}}$ . Assuming an emissivity equal to unity 1,  $Q_{\text{LW } \uparrow}^i = \sigma T_{\text{ice}}^4$  where  $\sigma = 5.67 \times 10^{-8} \text{ W m}^{-2} \text{ K}^{-4}$  is the Stefan-Boltzmann constant. This leads to  $Q_{\text{LW}}^i = Q_{\text{LW atm } \downarrow}^i - \sigma T_{\text{ice}}^4$  where  $\sigma = 5.67 \times 10^{-8} \text{ W m}^{-2} \text{ K}^{-4}$  is the Stefan-Boltzmann constant. The long wave flux received from the atmosphere  $Q_{\text{LW atm } \downarrow}^i$  is given by the meteorological S2M reanalysis model.

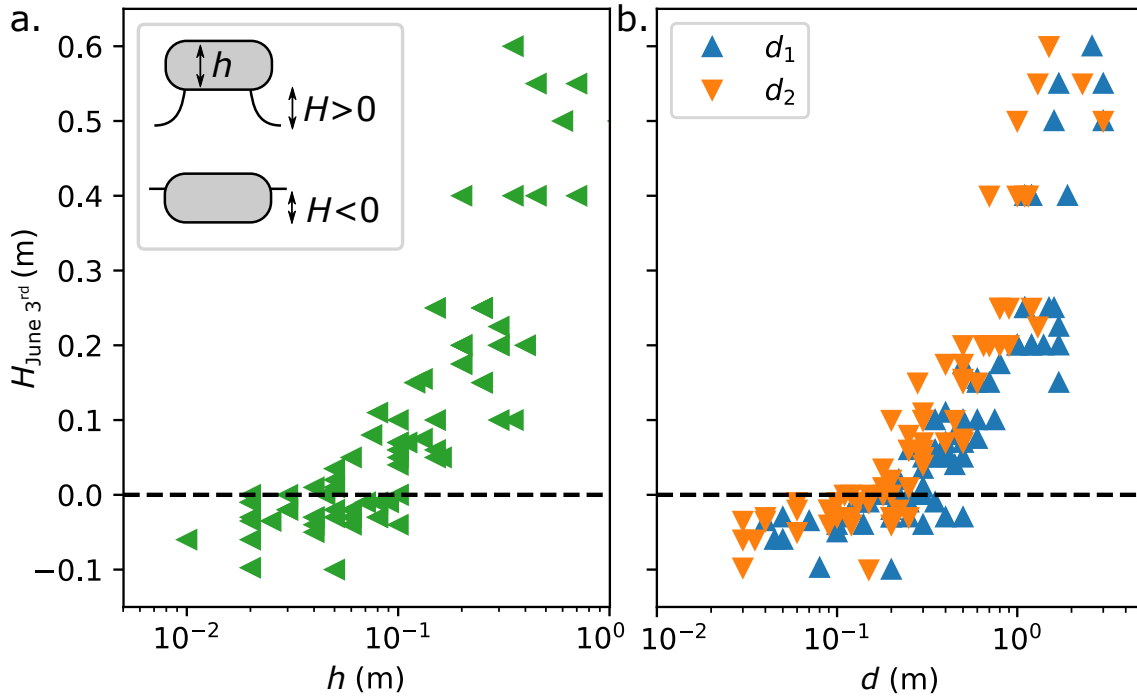


**Figure 3.** Raw data of the observation made at location 1 (see fig. 2a) on June 3<sup>rd</sup> 2021 : height of the ice foot ( $H > 0$ ) or of the penetration depth of the rock in the ice ( $H < 0$ ) as a function of the rock thickness  $h$  (a) and widths  $d_1$  and  $d_2$  (b). At the date of these observations the rocks were still standing on their ice feet and the maximum heights were presumably not reached yet.

The turbulent fluxes transmitted to a surface are assumed to be proportional to the wind velocity  $u_a$ :

$$Q_H^i = \rho_a c_p C_H u_a (T_{a,z_m} - T_{\text{surface}}) \quad (2)$$

$$Q_L^i = \rho_a L_v C_L u_a (q_{a,z_m} - q_{\text{surface}}) \quad (3)$$

115 where  $\rho_a = 0.98 \text{ kg m}^{-3}$  is the air density at atmospheric pressure at a 2100 m altitude  $p_{\text{atm}} = 785 \text{ hPa}$ ,  $c_p = 1004 \text{ J K}^{-1} \text{ kg}^{-1}$  is the specific heat capacity of air,  $L_v = 2.48 \text{ MJ kg}^{-1}$  is the latent heat of evaporation for water,  $T_{a,z_m}$  and  $q_{a,z_m}$  are respectively the air temperature and specific humidity at the height  $z_m$  above the surface. The specific humidity at the ice surface  $q_{\text{surface}} = q_{\text{ice}}$  is given by  $0.622 p_{\text{vap}}(T_{\text{ice}})/p_{\text{atm}}$  where  $p_{\text{vap}}(T_{\text{ice}}) = 611 \text{ Pa}$  is the vapour pressure of water at temperature  $T_{\text{ice}}$  (here and in the following  $p_{\text{vap}}(T)$  are obtained following the ITS-90 formula for water (Hardy, 1998)). The exchange

120 coefficients  $C_H$  and  $C_L$  are assumed to be identical and given by the simplest form found classically in the literature assuming a neutral atmospheric stability (Conway and Cullen, 2013):

$$C_H = C_L = \frac{k^2}{(\ln(z_m/z_0))^2} \quad (4)$$

where  $k = 0.41$  is the von Kármán constant and  $z_0$  is a roughness length characterizing the surface (assumed to be equal for the momentum, temperature and vapour pressure). This length is denoted as  $z_{0 \text{ ice}}$  for the ice surface. There were no precipitation



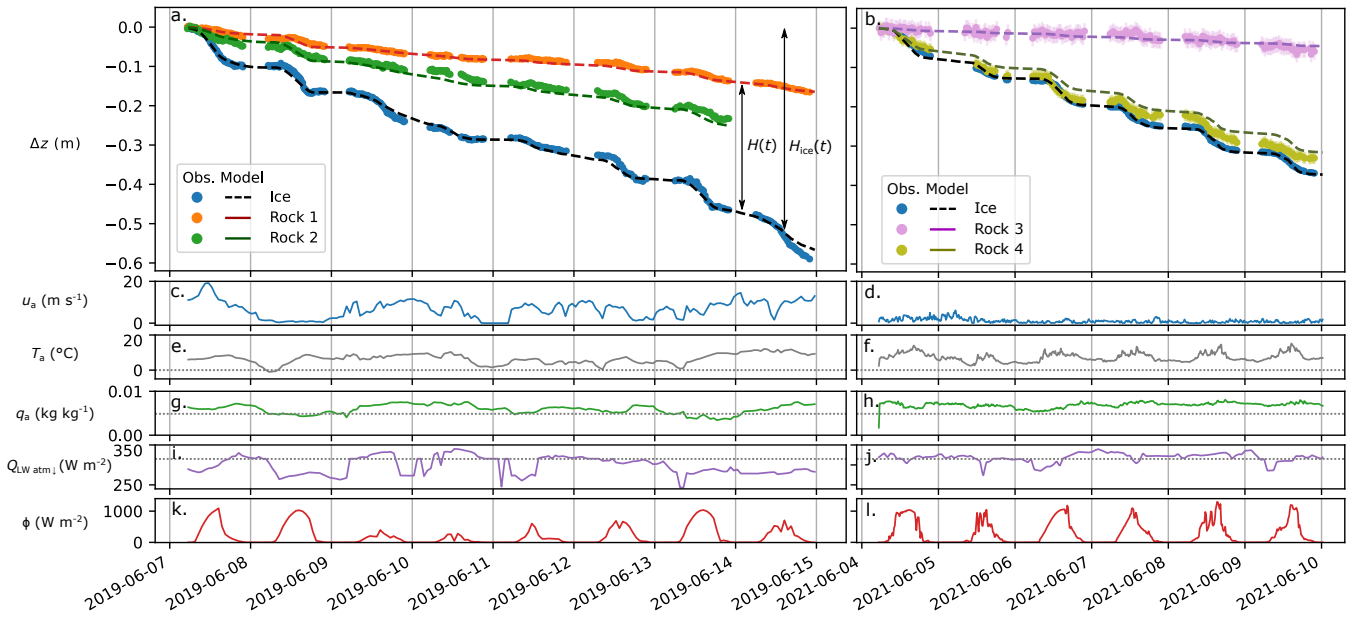


**Figure 4.** (a, b) Vertical position of the ice surface (blue markers), and of rocks 1 to 4 (colored markers, see table 1). The black dashed line corresponds to the model for ice ablation (see section 3.1). The colored solid lines correspond to the model for rocks (see section 3.2). These models use as input meteorological data measured at the Requin AWS: wind speed  $u_a$  (c, d), air temperature  $T_a$  (e, f), air specific humidity  $q_a$  (g, h) and solar radiation  $\Phi$  (k, l) as well as the longwave radiation coming from the atmosphere  $Q_{LW\ atm\ \downarrow}$  obtained from the S2M reanalysis (i, j). The dotted lines correspond to the ice surface values.

125 and thus no associated heat flux on the glacier during the duration of our study ( $Q_R^i = 0$ ). As the incoming heat flux directly causes the ice to melt, the vertical position of the ice surface  $z_{ice}(t)$  and the total ablated thickness of ice since  $t = 0$ ,  $H_{ice}(t)$ , are given by:

$$z_{ice}(t) - z_{ice}(0) = -H_{ice}(t) = -\mathcal{L}_{fus} \int_0^t Q_{\rightarrow ice}(t) dt \quad (5)$$

130 where  $\mathcal{L}_{fus} = 303\text{ MJ m}^{-3}$  is the volumetric enthalpy of fusion for ice. This model relies on meteorological data and has two adjustable parameters: the ice surface roughness  $z_{0\ ice}$  and its albedo  $\alpha_{ice}$ . These adjustable parameters will be determined from the model fit to the ice ablation rate measured away from the glacier tables in Section 4.1.

### 3.2 Glacier table formation model

In (Hénot et al., 2021), an analytical model was developed in order to explain the formation of artificial glacier tables made of cylindrical caps in a controlled environment, in which the heat transfer (natural convection of air and infrared radiation from the enclosure) was modelled through an effective heat exchange coefficient. In the following, we adapt this model to the non-symmetrical geometry of the rocks and we take into account the more complex energy balance of the glacier. Here we

only attempt to describe the vertical motion of the rock with respect to the ice surface and we do not consider the lateral melt of the ice foot in this model, but this is briefly discussed in conclusion.

For the sake of simplicity, the following main assumptions are made in the model: (1) the rocks are considered as cuboids (see fig. 2b). The area  $A_{\text{base}}$  of contact with the ice is considered constant during the table formation, although it evidently varies over time. Yet, as discussed in the supplementary material, this has little effect on the total heat transfer. The top and bottom areas are thus  $A_{\text{top}} = A_{\text{bottom}} = d_1 d_2$  and the side area is  $A_{\text{side}} = 2(d_1 + d_2)h$ . (2) The surface temperature of the rock is assumed homogeneous and is denoted as  $T_{\text{rock}}$  allowing the development of a 1D thermal conduction model. (3) The thermal process is assumed to be quasi-static, meaning that all transient thermal effects are neglected. The validity of this assumption is discussed in the supplementary materials.

The energy balance of a rock, taking into account its 3D structure, is summarized in the schematic of fig. 5a. The shortwave radiative flux is received by the rock on a surface  $\langle A_{\text{sun}} \rangle$ . This area should depend on the shape and orientation of the rock with respect to the course of the sun, but for sake of simplicity in the following it is simply assumed to be equal to the rock base surface area  $\langle A_{\text{sun}} \rangle = A_{\text{base}}$  (the validity of this assumption is discussed in the suppl. mat.). The longwave flux coming from the atmosphere  $Q_{\text{LW atm } \downarrow}$  is also assumed to be received only on the top surface of area  $A_{\text{base}}$  but the rock also receives on its side a longwave flux denoted as  $Q_{\text{LW env } \downarrow}$ . Strictly speaking this quantity depends on the emissivity, surface temperature and view factor of all surfaces (ice, other rocks, terrain) seen from the rock sides (Lienhard, 2019) and thus cannot be simply estimated. In the following it will be kept as an adjustable parameter. The rock also emits a longwave flux  $Q_{\text{LW } \uparrow}^r$  from its external surface (top and side). The sensible and latent fluxes  $Q_{\text{H}}^r + Q_{\text{L}}^r$  are received from the air on the external surface of the rock (of area  $A_{\text{base}} + A_{\text{side}}$ ). Finally a flux  $Q_{\text{rock} \rightarrow \text{ice}}$  is transferred to the ice through the contact area  $A_{\text{base}}$ .

The quasi-static assumption implies that the flux balance is verified at each time:

$$A_{\text{base}} Q_{\text{rock} \rightarrow \text{ice}} = A_{\text{top}} Q_{\text{SW}}^r + A_{\text{base}} (Q_{\text{LW atm } \downarrow} - Q_{\text{LW } \uparrow}^r) + A_{\text{side}} (Q_{\text{LW env } \downarrow} - Q_{\text{LW } \uparrow}^r) + (A_{\text{base}} + A_{\text{side}}) (Q_{\text{H}}^r + Q_{\text{L}}^r) \quad (6)$$

The net shortwave flux is  $Q_{\text{SW}}^r = (1 - \alpha_{\text{rock}}) \Phi$  where  $\alpha_{\text{rock}} = 0.18$  is the albedo of the granite rock (measured by (Watson, 1971), see the supplementary material). The granite emissivity is taken equal to 1 (Michalski et al., 2004) leading to  $Q_{\text{LW } \uparrow}^r = \sigma T_{\text{rock}}^4$ . The turbulent fluxes are computed according to an equation similar to equation 3, for which the surface terms are those relative to the rock, i.e.  $T_{\text{surface}} = T_{\text{rock}}$ ,  $q_{\text{surface}} = 0.622 p_{\text{vap}}(T_{\text{rock}}) / p_{\text{atm}}$  and  $z_0 = z_0_{\text{rock}}$ . If  $Q_{\text{L}} > 0$  water from the air condenses on the rock surface, which justifies the value of  $q_{\text{surface}}$  (corresponding to 100 % humidity at the temperature  $T_{\text{rock}}$ ). However,  $Q_{\text{L}} < 0$  would correspond to evaporation and would be limited by the quantity of water present on the rock surface. In the following  $Q_{\text{L}}$  is thus forced to 0 if  $Q_{\text{L}} < 0$ .

The heat flux transmitted from the rock to the ice underneath can be estimated using a 1D conduction model as:

$$Q_{\text{rock} \rightarrow \text{ice}} = \lambda \frac{(T_{\text{rock}} - T_{\text{ice}})}{d_{1\text{D}}} \quad (7)$$

where  $\lambda$  is the thermal conductivity of granite (measured in a previous work (Hénot et al., 2021) as  $\lambda = 2.8 \text{ W m}^{-1} \text{ K}^{-1}$ , which is in agreement with the literature (Cho et al., 2009)) and  $d_{1\text{D}}$  is a length scale for the conduction process in the rock. It was postulated, and verified experimentally (see fig. 5 of Hénot et al. (2021)), that this length could be estimated



170 by  $d_{1D} = \eta \frac{V_{\text{rock}}}{A_{\text{ext}}} = \eta \frac{e}{1+4\beta}$  where  $V_{\text{rock}}$  is the volume of the rock and  $\eta = 2.5$  is a numerical prefactor adjusted from the lab experiments.

From eq. 6 and 7 and using the measured meteorological data ( $\Phi(t)$ ,  $Q_{\text{LW atm } \downarrow}(t)$ ,  $u_a(t)$ ,  $T_a(t)$  and  $q_a(t)$ ) as input, the rock surface temperature  $T_{\text{rock}}(t)$  can be computed at each time  $t$  by solving numerically non-linear equation 6. The flux  $Q_{\text{rock} \rightarrow \text{ice}}(t)$  reaching the ice can then be computed. When positive, this leads to ice melting under the rock, lowering the  
 175 altitude of the bottom of the rock  $z_{\text{rock}}$ :

$$z_{\text{rock}}(t) - z_{\text{ice}}(0) = -\mathcal{L}_{\text{fus}} \int_0^t Q_{\text{rock} \rightarrow \text{ice}}(t) dt \quad (8)$$

The height of the ice foot supporting the rock is  $H(t) = z_{\text{rock}}(t) - z_{\text{ice}}(t)$ . The time origin corresponds to the rock lying at the surface of the ice ( $H(t=0) = 0$ ). Note that at this stage, there are two adjustable parameters in the table formation model:  $Q_{\text{LW env } \downarrow}$  and  $z_{0 \text{ rock}}$  ( $\alpha_{\text{rock}}$  and  $\eta$  are taken from the literature). However, the roughness size  $z_0$  in the turbulent coefficient is  
 180 not clearly defined defined (Hock, 2005) but the resulting model is not very sensible to its value. Thus in the following,  $z_{0 \text{ rock}}$  will be taken equal to that of the ice  $z_{0 \text{ ice}}$ .

## 4 Results

### 4.1 Ice melting

The daily ice ablation rate was a little bit different on period A and B: on clear-sky days it was of the order of  $8 \text{ cm day}^{-1}$   
 185 on period A (3/8 clear-sky days) and  $5.5 \text{ cm day}^{-1}$  on period B (5/5 clear-sky days). The black dashed lines in fig. 4a and b correspond to the model described in section 3.1 with parameters  $\alpha_{\text{ice}} = 0.30$  and  $z_0 = 0.34 \text{ mm}$  adjusted on the concatenated data of periods A and B (see the supplementary material for a discussion on the sensibility). The agreement between the model and the field measurements is good: the error on  $z_{\text{ice}}(t)$  stays below 3 cm (except at the end of period A when the movement of the camera increases the uncertainty on the measurements). The value of the adjusted ice albedo corresponds to what is reported  
 190 in the literature for aged surface glacier ice, at the beginning of summer (Brock et al., 2000). The value of the roughness length  $z_0$  also falls in the range previously reported ( $10^{-4} - 10^{-2} \text{ m}$ ) (Brock et al., 2006; Conway and Cullen, 2013). Fig. 5 shows (in white) the time averaged values of  $Q_{\text{SW}}^i$ ,  $Q_{\text{LW}}^i$ ,  $Q_{\text{H}}^i$ ,  $Q_{\text{E}}^i$  as well as the total flux reaching the ice surface:  $Q_{\text{open env} \rightarrow \text{ice}}$  for both time periods. The shortwave flux varies weakly between periods A and B (from  $150$  to  $200 \text{ W m}^{-2}$ ) and the net longwave flux is comparatively small ( $-20$  to  $3 \text{ W m}^{-2}$ ). The total turbulent flux  $Q_{\text{H}}^i + Q_{\text{E}}^i$ , strongly differs between periods A and B.  
 195 It decreases from  $120 \text{ W m}^{-2}$  (which represents 50 % of the total flux) in period A to  $25 \text{ W m}^{-2}$  (10 % of the total flux) in period B. This is due to the drastic difference in mean wind speed, from  $6.5 \text{ m s}^{-1}$  during period A to  $1.0 \text{ m s}^{-1}$  during period B, which explains the difference in ice ablation rate.

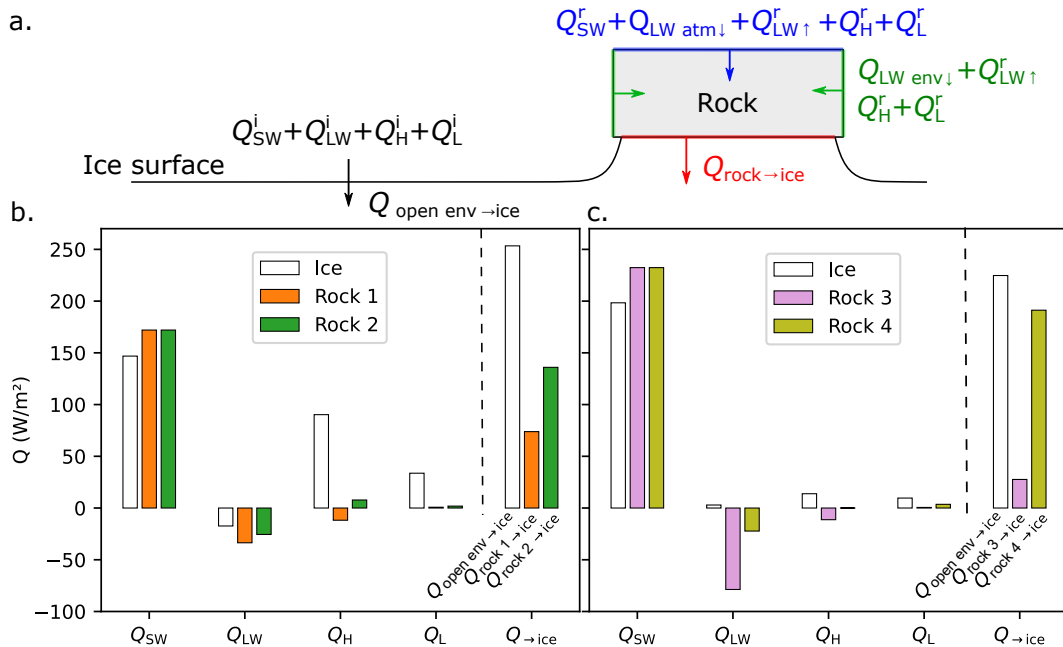


**Figure 5.** (a) Schematics of the heat fluxes considered in the models for the ice surface melting (left) and glacier table formation. The colors denotes the surfaces on which the fluxes are received. (b, c) Distribution of the heat fluxes averaged over the duration of observation as predicted by the time resolved model for the ice surface (white) and for the 4 rocks studied (colored).

## 4.2 Table formation

Rocks 1 and 2 formed glacier tables over the course of approximately a week (see fig. 4a and b), after which they fell off the ice pedestal. Rock 3 was initially sitting on an ice foot, which grew bigger, while rock 4, although exhibiting dimensions close to those of rock 2 went down almost at the same rate as the bare ice surface and did not form any significant glacier table (see the supplementary material for pictures). The integration of the flux given by the model is shown in solid lines in fig. 4a and b. The best agreement with the observed data was obtained for a value of the adjustable parameter  $Q_{LW\ env\downarrow} = 340\ W\ m^{-2}$ . This corresponds to the longwave flux emitted by a surface with emissivity 1 at a temperature 278.3 K which seems reasonable as the physical meaning of this quantity is the mean temperature of the environment seen by the sides of the rocks (ice surface, others rocks and terrain surrounding the glacier). The agreement between the measurements and the model prediction is over all good for rocks 1 to 3. The model overestimate slightly the ability to form a table of rock 4 but the error (integrated over 6 days) stays under 3 cm for a total ice ablation of 37 cm. Fig. 6 shows the measured temperature of the top surface of rock 4 (solid line) as well as the value of  $T_{rock}(t)$  predicted by the model. The two curves qualitatively display the same behaviour. The mean temperature is slightly overestimated by the model on average (by 2°C) but the typical minimum (0-3°C) and maximum (22-24°C) daily temperature remain close.

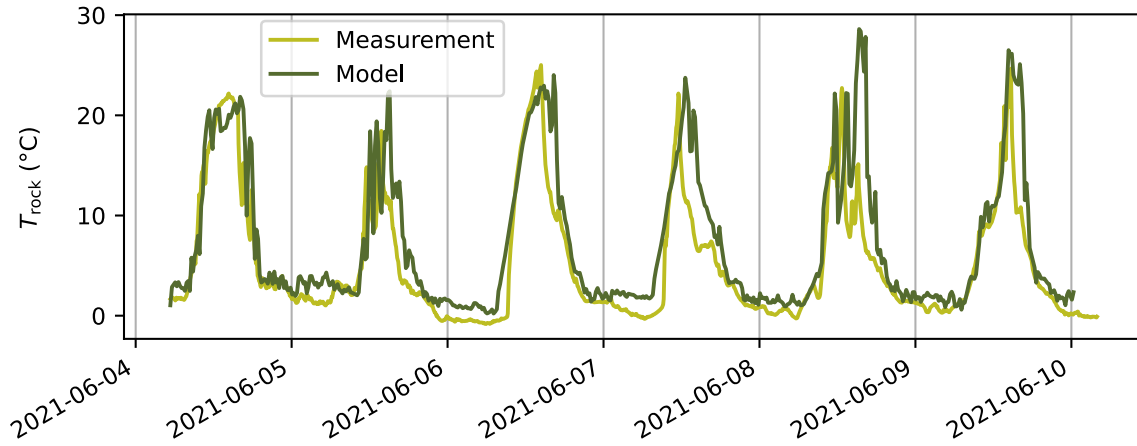


**Figure 6.** Temperature  $T_{\text{rock}}$  of the top surface of rock 4 measured using a thermocouple (light green) and predicted by the model using the meteorological data of period B (dark line).

Figure 5 shows for each rock (in color) the surface and time averaged radiative and turbulent flux computed from the model as well as the resulting heat flux transmitted to the ice underneath. The shortwave flux received on the top surface of the rocks is 17 % higher than the one received by the ice due to the difference in albedo. However the net longwave and turbulent flux are significantly reduced due to the fact that on average the rocks surface temperature  $\langle T_{\text{rock}} \rangle$  are higher than  $T_{\text{ice}}$ . For rocks 1 to 4, the averaged surface temperature predicted were respectively 8.2, 6.3, 13.0 and 7.2°C. The turbulent flux reduction is more important during period A than during period B due to the higher mean wind speed. Note that these reduction effect is geometrically amplified (by a factor  $1 + 4\beta$ ) as these negative flux are integrated over the external surface of the rocks which is larger than the base surface in contact with ice (this is especially true for rock 4 which has the largest aspect ratio). For all the rocks studied, the predicted flux causing ice to melt under the rocks was on average reduced compared to the flux received by the ice surface (from -15 % for rock 4 to -88 % for rock 3) leading to the formation of tables. Note that this amplification effect can also, depending of the shape and size of the rocks, have the opposite consequence of causing a rock to sink into the ice surface as it will be shown in section 5.2.

Fig. 7a shows for each rock, the height of the ice foot,  $H(t) = z_{\text{rock}}(t) - z_{\text{ice}}(t)$ , as a function of the ablated ice thickness,  $H_{\text{ice}}(t) = z_{\text{ice}}(t) - z_{\text{ice}}(0)$ . On average these quantities appear to be proportional. The slope corresponds to a dimensionless growth rate of the glacier table, denoted as  $\langle H/H_{\text{ice}} \rangle$ : a unity slope would correspond to no melt under the rock (the ice foot height would then correspond exactly to the ablated ice thickness), conversely a zero slope would correspond to a rock descending at the same rate as the ice surface around it and thus never forming a glacier table. The solid lines in fig. 7a correspond to linear adjustments. The deduced slopes  $\langle H/H_{\text{ice}} \rangle$  are plotted for each rock in fig. 7b as a function of their thickness  $h$  (markers). The value predicted by the model is plotted on the same figure for period A (dashed lines) and B (solid lines) for the values of  $\beta$  corresponding to the 4 rocks as a function of the thickness of the rock. Moving along a line thus corresponds to a change in scale but not in shape of the rocks. The dimensionless growth rates of the tables are accurately

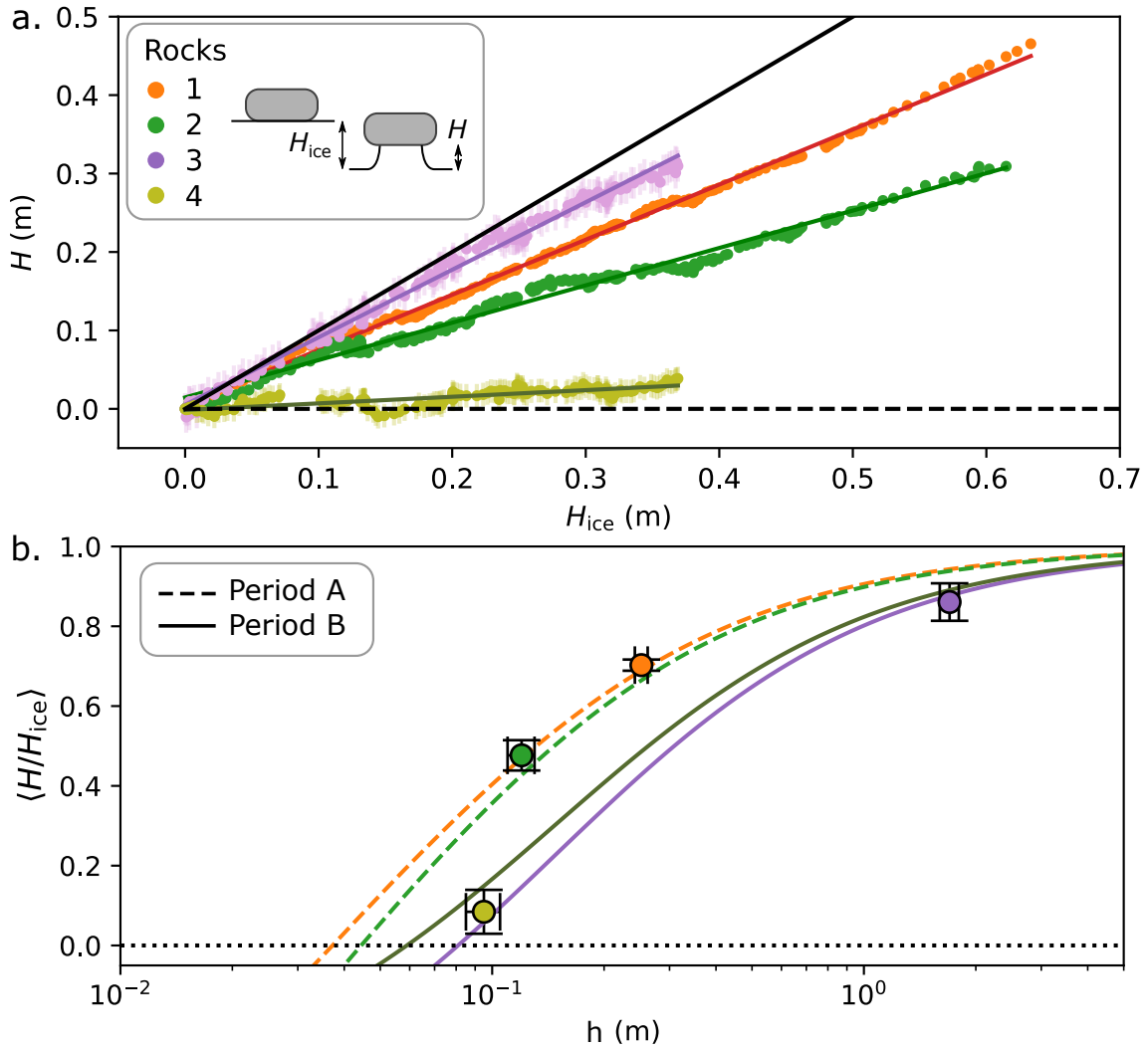


**Figure 7.** (a) Evolution of the height  $H$  of the ice foot under rocks 1-4 as a function of the ice ablated thickness  $H_{ice}$ . The colored lines correspond to linear adjustments of the data. The solid black line has a slope 1. (b) Mean ratio of the height  $H$  of the ice foot under a rock and of the total ablated ice thickness  $H_{ice}$  since the beginning of the table formation, as a function of the thickness  $h$  of the rock. The markers correspond to the slopes of fig. a for each rocks. The lines correspond to the application of the model for the meteorological values measured in period A (dashed lines) and B (solid lines) and the aspect ratio  $\beta$  of each rock given in table 1.

predicted by the model. It is visible that independently of the rock shape and time period, a small enough rock would not form a table and instead sink into the ice surface ( $\langle H/H_{ice} \rangle < 0$ ).

### 235 4.3 Analysis of the 80 glacier tables field

In figure 3 showing the height of the ice structure formed by 80 rocks 8 days after the melt of the snow layer, is it visible that it exists is a critical size (4-10 cm in thickness and 9-13 cm in width) above which rocks tend to form glacier tables. The larger the rock, the greater its ability to protect the ice underneath from melting and, assuming all tables started their formation at the same time, the higher the ice foot. Below this critical size, however, the rocks have a tendency to sink into the ice surface.

240 Having successfully modelled the evolution of the 4 larger glacier tables, the model presented in section 3.2 can be applied to the data obtained on a given day for a field comprising 80 rocks.

The snow layer covering that part of the glacier finished melting on May 26, leaving the ice exposed. The meteorological data of the time period C (from May 26 until June 3), alongside with the previously adjusted parameters  $\alpha_{ice}$  and  $z_0$  allows to compute the thickness of ablated ice  $H_{ice} = 0.45 \pm 0.05$  m during this period (see fig. S5 of the supplementary material).

245 The observed values of  $H$  are plotted on fig. 8a as a function of the ones predicted by the model for each rock assuming that the structure formation started on May 26 ( $H_{May26} = 0$ ). The rocks that have sunken into the ice surface ( $H < 0$ ) are shown in blue. For those, the prediction of the model is, as expected, not accurate. Indeed, a rock that has penetrated into the ice has a greater contact surface area with the ice and a smaller external surface open to atmosphere than what is taken into account in the model. It is thus cooler and its (negative) dimensionless growth rate is smaller (in absolute terms) than that given by the model, as observed. The rocks that have formed glacier tables ( $H > 0$ ) are shown in red. The threshold between rocks forming or not a table (the point (0,0) in the graph) is well predicted by the model. For the smaller structures ( $H < 0.3$  m), the height of the ice foot is also well predicted (with an error smaller than 5 cm). Note that this required no new adjustable parameter and this prediction is the result of a model integrated over 8 days on a time period different from A and B, during which the parameters of the model were adjusted. For ice feet taller than 0.3 m however the prediction of the model is not good. For 255 some,  $H > H_{ice}$  and the assumption  $H_{May26} = 0$  is thus obviously not valid. We infer that larger rocks emerged from the snow layer before May 26 and started to form a table earlier.

## 5 Discussion

### 5.1 Critical diameter

The critical diameter, corresponding to the transition between the two regimes described in the previous section (the rock 260 sinks into the ice or forms a table), is denoted as  $d_{crit}$ . We chose to consider a critical width instead of a critical thickness as the transition seems sharper when considering this quantity in fig. 3. This is reminiscent of the results obtained in a controlled environment in the absence of solar radiation, for which the transition occurred for a critical diameter of the cylinders, independently of their aspect ratio (Hénot et al., 2021).

From our model, given a set of meteorological data and an aspect ratio  $\beta$ , a critical width  $d_{crit}$  can be computed. In the 265 following, unlike what was done until then, typical time-averaged meteorological data ( $\langle \Phi \rangle = 210 \text{ W m}^{-2}$ ,  $\langle Q_{LW \text{ atm } \downarrow} \rangle = 315 \text{ W m}^{-2}$ ,  $\langle T_a \rangle = 7^\circ\text{C}$ ,  $\langle q_a \rangle = 0.0058 \text{ kg kg}^{-1}$  and  $\langle u_a \rangle$  ranging from 0 to 20  $\text{m s}^{-1}$ ) will be used as inputs (we have

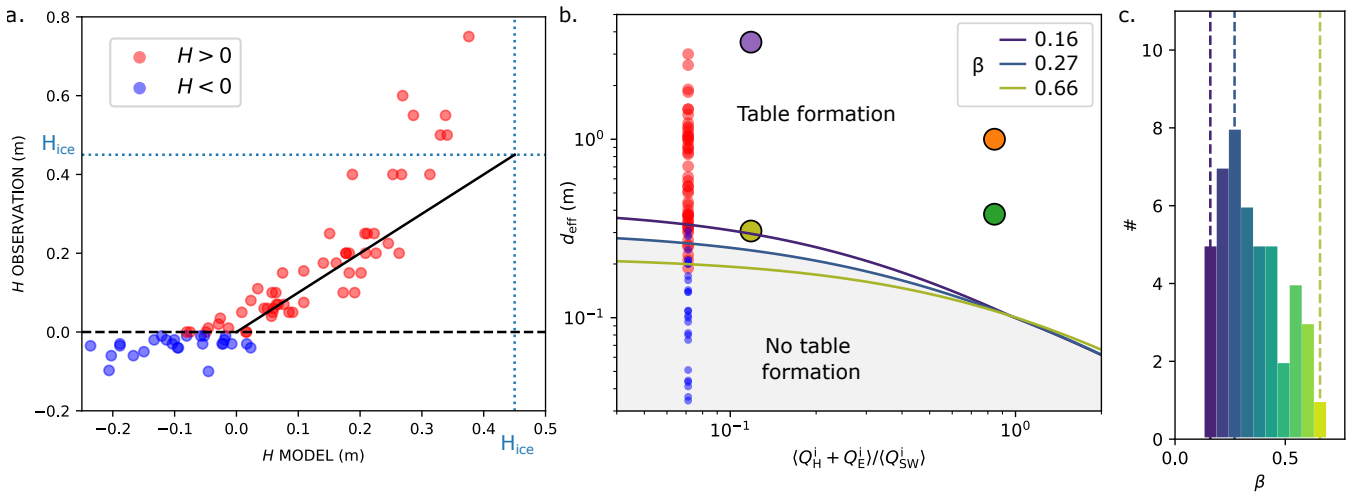


**Figure 8.** (a) Observation versus model for the distance  $H$  between the bottom of rocks and the ice surface for the data measured on June 3<sup>rd</sup> 2021 (see fig. 3). The data are represented in red if a table is observed ( $H > 0$ ) and in blue otherwise. The solid black line has a slope 1 and the dotted lines correspond to the ablated ice thickness  $H_{ice}$  since the melting of the snow layer (see the supplementary material). (b) Diagram of the ability for a rock to form a table as a function of its typical width  $d_{eff}$  and the ratio  $\langle Q_H^i + Q_E^i \rangle / \langle Q_{SW}^i \rangle$ . The solid lines corresponds, for three values of the aspect ratio  $\beta$  to the delimitation predicted by the model with averaged meteorological data, between a rock forming a table and a rock sinking into the ice surface. The small circles correspond to the data of (a) with the same color code. The larger circles correspond to rocks 1-4. (c) Distribution of the aspect ratio  $\beta$  of the rocks close to the transition between the two regimes ( $|H| < 0.2$  m). The vertical dashed lines correspond to the limits plotted in fig. b. with the same color code.

checked that this pre-averaging of the input data affects the output of the model by less than a few percents). Fig. 8b shows a diagram of the ability for a rock to form a table as a function of its effective width  $d_{eff}$  (which in practice can be replaced by the mean width) and the ratio  $\langle Q_H^i + Q_E^i \rangle / \langle Q_{SW}^i \rangle$ , which is a quantity proportional to  $\langle u_a \rangle$  and whose relevance will be  
270 discussed in the next paragraph. The four monitored rocks as well as the field data from the 80 rocks found in the 800-m<sup>2</sup> field are plotted in this diagram. The distribution of aspect ratio  $\beta$  of rocks (46 of them) close to the transition (defined by  $|H| < 0.2$  m) is plotted in fig.8c. The bounding values ( $\beta = 0.16$  and  $0.66$ ) as well as the value corresponding to the maximum of the distribution ( $\beta = 0.27$ ) are used to plot in fig. 8b the values of  $d_{crit}$  predicted by the model. This threshold, which depends slightly on  $\beta$ , shows a good agreement with the transition visible in the field data. This diagram illustrates the sensibility of the  
275 glacier table formation to the meteorological conditions and especially the mean wind speed:  $d_{eff}$  is divided by two between time periods A and B.

## 5.2 Physical discussion

A rock forms a glacier table when the heat flux reaching the ice underneath is reduced compared to that received by the bare ice surface around it. If, on the contrary, this heat flux is amplified, the rock will sink into the ice surface. Depending on the rock

280 size, both phenomena are observed on temperate glaciers. During summer, the main source of heat flux causing the ice to melt is the shortwave radiation coming from the sun. Due to the lower albedo of the rock, this flux is slightly amplified compared to what is received by a similar area of bare ice and thus does not directly favor the formation of glacier tables. However this induces a heat flux across the thickness of the rock that elevates its surface temperature  $T_{\text{rock}}$  (the bottom surface staying at  $T_{\text{ice}}$ ). This strongly affects the net infrared radiation and turbulent fluxes which otherwise play a minor role in the surface ice  
 285 melting (especially for the later when the wind is calm). As can be seen in fig. 5, the sign of the sensible flux can even change (if  $T_{\text{rock}} > T_a > T_{\text{ice}}$ , the wind warms the ice surface but cools the rock) and induces a negative net shortwave flux (the rock flux lost being proportional to  $T_{\text{rock}}^4$ ). At the end, if the rock is large enough (so that its surface temperature can rise enough), all these combined effects lead to the formation of a glacier table. As illustrated by the difference between periods A and B, the wind intensity can vary significantly at the surface of the glacier. The sensible flux being one motor of glacier table formation  
 290 (with emitted longwave radiation), this affects the critical size  $d_{\text{crit}}$ . The ratio  $\langle Q_{\text{H}}^i + Q_{\text{E}}^i \rangle / \langle Q_{\text{SW}}^i \rangle$  used in abscissa in fig. 8b. demonstrates this effect. When this ratio is small ( $< 0.1$ ), the structure formation is controlled by the longwave emission of the rock, while a large value ( $> 1$ ) would correspond to a regime dominated by the effect of sensible flux. Note that at this point, a 1D model with  $d_{1\text{D}} = h$  and no geometrical amplification would have achieved the same result. However, the 3D structure has its importance: the heat transfer with the environment (shortwave and turbulent) that cools the rock is exchanged on a surface  
 295 area with is much larger than the base area of a rock. In our model we considered the total external surface of the rock, which is larger by a factor  $1 + 4\beta$  typically of order 2-3 than  $A_{\text{base}}$ . As detailed in the supplementary materials, a 1D model would, in order to verify eq. 6 significantly overestimate  $T_{\text{rock}}$  (by  $150^\circ\text{C}$  during sunlight for rock 3, which is not a physically acceptable value). This 3D effect also explains the influence of the rock shape on its ability to form a table.

The formation of glacier tables in the natural environment of a temperate glacier results from a more complex energy balance  
 300 than the idealized lab-controlled study conducted previously (Hénot et al., 2021) while the main physical ingredient stays the same: the greater temperature of the rock surface, compared to the ice, reduces the incoming heat flux and thus the melt rate under the rock. In the absence of solar radiation, the threshold controlling the ability for a rock to form a table was determined by a trade-off between this effect and a geometrical amplification effect: a rock can act as a fin in amplifying the incoming heat flux leading to a higher melt rate under the rock than for bare ice. While this effect also plays a role in natural condition, the  
 305 threshold is also significantly affected by the direct solar radiation that has two opposite effects: on the one hand, due to lower albedo, a higher flux is received by a rock than a bare ice surface but, on the other hand, the temperature gradient induced by the solar flux across a rock elevates its temperature, enhancing the cooling effect due to turbulent and longwave flux. The first effect dominates for small rocks while the later dominates for larger rocks.

## 6 Conclusions

310 We studied the formation of four glacier tables over the course of a week and we measured the characteristics of 80 glacier tables on the Mer de Glace (Alps). We found out that the size of the rocks is a determinant factor governing table formation: the bigger the rock, the higher and faster the ice foot supporting it will grow. Under a critical size, rocks show the opposite



behaviour of sinking into the ice surface. We developed a simple model taking into account the infrared and solar radiation and turbulent heat flux received by a rock and by the glacier ice surface using local meteorological data allowing to identify the physical effects controlling the structure formation. While the heat transfer across the rock controls for the formation dynamics, the end of life of glacier tables and in particular the maximum height reached by ice feet will likely result from lateral melting of the ice column. This process is expected to be affected by the rock shape and size that would prevent radiative melting due to shading effect, leaving only turbulent flux and longwave balance. Note also that when the ice pedestal becomes very slender, a heavy rock could also causes the ice column to creep. These aspects were not considered in this study but could be the subject of future work.

*Author contributions.* MH, VL, NP and NT conceived the study and performed the fieldwork. MH performed the data analysis, developed the model and drafted the manuscript. All authors contributed to the data interpretation, discussion of the results and writing of the manuscript.

*Competing interests.* The authors declare that they have no conflict of interest.

*Acknowledgements.* This study received financial support from the Fédération de Recherche André Marie Ampère and Laboratoire de Physique at ENS de Lyon. The authors acknowledge technical support and useful scientific discussion with Marine Vicet, Jérémy Vessaire and Thierry Dauxois. The S2M data are provided by Météo-France CNRS, CNRM Centre d'Etudes de la Neige, through AERIS.

## References

- Agassiz, L.: Études sur les glaciers, Gent & Gassman, Neuchâtel, 1840.
- Bergeron, V., Berger, C., and Betterton, M. D.: Controlled Irradiative Formation of Penitentes, *Physical Review Letters*, 96,  
330 <https://doi.org/10.1103/physrevlett.96.098502>, 2006.
- Betterton, M. D.: Theory of structure formation in snowfields motivated by penitentes, suncups, and dirt cones, *Phys. Rev. E*, 63, 056 129,  
<https://doi.org/10.1103/PhysRevE.63.056129>, 2001.
- Bintanja, R., Reijmer, C. H., and Hulscher, S. J. M. H.: Detailed observations of the rippled surface of Antarctic blue-ice areas, *Journal of  
Glaciology*, 47, 387–396, <https://doi.org/10.3189/172756501781832106>, 2001.
- 335 Bordiec, M., Carpy, S., Bourgeois, O., Herny, C., Massé, M., Perret, L., Claudin, P., Pochat, S., and Douté, S.: Sublimation  
waves: Geomorphic markers of interactions between icy planetary surfaces and winds, *Earth-Science Reviews*, 211, 103 350,  
<https://doi.org/10.1016/j.earscirev.2020.103350>, 2020.
- Bouillette, E.: Une Superbe Table des Glaciers, *L'Astronomie*, 47, 201–202, 1933.
- Bouillette, E.: La fin d'une table des glaciers, *L'Astronomie*, 48, 89–91, 1934.
- 340 Brock, B. W., Willis, I. C., and Sharp, M. J.: Measurement and parameterization of albedo variations at Haut Glacier d'Arolla, Switzerland,  
*Journal of Glaciology*, 46, 675–688, <https://doi.org/doi:10.3189/172756500781832675>, 2000.
- Brock, B. W., Willis, I. C., and Sharp, M. J.: Measurement and parameterization of aerodynamic roughness length variations at Haut Glacier  
d'Arolla, Switzerland, *Journal of Glaciology*, 52, 281–297, <https://doi.org/10.3189/172756506781828746>, 2006.
- Bruthans, J., Soukup, J., Vaculikova, J., Filippi, M., Schweigstillova, J., Mayo, A. L., Masin, D., Kletetschka, G., and Rihosek, J.: Sandstone  
345 landforms shaped by negative feedback between stress and erosion, *Nature Geoscience*, 7, 597–601, <https://doi.org/10.1038/ngeo2209>,  
2014.
- Bushuk, M., Holland, D. M., Stanton, T. P., Stern, A., and Gray, C.: Ice scallops: a laboratory investigation of the ice–water interface, *Journal  
of Fluid Mechanics*, 873, 942–976, <https://doi.org/10.1017/jfm.2019.398>, 2019.
- Carenzo, M., Pellicciotti, F., Mabillard, J., Reid, T., and Brock, B. W.: An enhanced temperature index model for debris-covered glaciers  
350 accounting for thickness effect, *Advances in Water Resources*, 94, 457–469, <https://doi.org/10.1016/j.advwatres.2016.05.001>, 2016.
- Cho, W., Kwon, S., and Choi, J.: The thermal conductivity for granite with various water contents, *Engineering Geology*, 107, 167 – 171,  
<https://doi.org/https://doi.org/10.1016/j.enggeo.2009.05.012>, 2009.
- Claudin, P., Jarry, H., Vignoles, G., Plapp, M., and Andreotti, B.: Physical processes causing the formation of penitentes, *Physical Review E*,  
92, <https://doi.org/10.1103/physreve.92.033015>, 2015.
- 355 Claudin, P., Durán, O., and Andreotti, B.: Dissolution instability and roughening transition, *Journal of Fluid Mechanics*, 832,  
<https://doi.org/10.1017/jfm.2017.711>, 2017.
- Cohen, C., Berhanu, M., Derr, J., and du Pont, S. C.: Erosion patterns on dissolving and melting bodies, *Physical Review Fluids*, 1, 050 508,  
<https://doi.org/10.1103/PhysRevFluids.1.050508>, 2016.
- Cohen, C., Berhanu, M., Derr, J., and Du Pont, S. C.: Buoyancy-driven dissolution of inclined blocks: Erosion rate and pattern formation,  
360 *Physical Review Fluids*, 5, 053 802, <https://doi.org/10.1103/PhysRevFluids.5.053802>, 2020.
- Collier, E., Nicholson, L., Brock, B., Maussion, F., Essery, R., and Bush, A.: Representing moisture fluxes and phase changes in glacier  
debris cover using a reservoir approach, *The Cryosphere*, 8, 1429–1444, <https://doi.org/10.5194/tc-8-1429-2014>, 2014.

- Conway, J. and Cullen, N.: Constraining turbulent heat flux parameterization over a temperate maritime glacier in New Zealand, *Annals of Glaciology*, 54, 41–51, <https://doi.org/10.3189/2013AoG63A604>, 2013.
- 365 Drewry, D. J.: A Quantitative Assessment of Dirt-Cone Dynamics, *Journal of Glaciology*, 11, 431–446, <https://doi.org/10.3189/S0022143000022383>, 1972.
- Evatt, G., Mayer, C., Mallinson, A., Abrahams, I., Heil, M., and Nicholson, L.: The secret life of ice sails, *Journal of Glaciology*, 63, 1049 – 1062, <https://doi.org/10.1017/jog.2017.72>, 2017.
- Evatt, G. W., Abrahams, I. D., Heil, M., Mayer, C., Kingslake, J., Mitchell, S. L., Fowler, A. C., and Clark, C. D.: Glacial melt under a porous debris layer, *Journal of Glaciology*, 61, 825–836, <https://doi.org/10.3189/2015JoG14J235>, number: 229, 2015.
- 370 Fitzpatrick, N., Radić, V., and Menounos, B.: Surface Energy Balance Closure and Turbulent Flux Parameterization on a Mid-Latitude Mountain Glacier, Purcell Mountains, Canada, *Frontiers in Earth Science*, 5, 67, <https://doi.org/10.3389/feart.2017.00067>, 2017.
- Fowler, A. C. and Mayer, C.: The formation of ice sails, *Geophysical & Astrophysical Fluid Dynamics*, 111, 411–428, <https://doi.org/10.1080/03091929.2017.1370092>, 2017.
- 375 Guérin, A., Derr, J., Du Pont, S. C., and Berhanu, M.: Streamwise dissolution patterns created by a flowing water film, *Physical Review Letters*, 125, 194 502, <https://doi.org/10.1103/PhysRevLett.125.194502>, 2020.
- Hardy, B.: ITS-90 Formulations for Vapor Pressure, Frost point Temperature, Dew point Temperature, and Enhancement Factors in the range –100 to +100 C”, *Papers and Abstracts of the Third International Symposium on Humidity and Moisture*, pp. 214–222, 1998.
- Hénot, M., Plihon, N., and Taberlet, N.: Onset of Glacier Tables, *Phys. Rev. Lett.*, 127, 108 501, <https://doi.org/10.1103/PhysRevLett.127.108501>, 2021.
- 380 Hock, R.: Glacier melt: a review of processes and their modelling, *Progress in Physical Geography: Earth and Environment*, 29, 362–391, <https://doi.org/10.1191/0309133305pp453ra>, number: 3, 2005.
- Huang, J. M., Tong, J., Shelley, M., and Ristorph, L.: Ultra-sharp pinnacles sculpted by natural convective dissolution, *Proceedings of the National Academy of Sciences*, 117, 23 339–23 344, <https://doi.org/10.1073/pnas.2001524117>, 2020.
- 385 Huinink, H. P., Pel, L., and Kopinga, K.: Simulating the growth of tafoni, *Earth Surface Processes and Landforms*, 29, 1225–1233, <https://doi.org/10.1002/esp.1087>, 2004.
- Krenek, L. O.: The Formation of Dirt Cones on Mount Ruapehu, New Zealand, *Journal of Glaciology*, 3, 312–315, <https://doi.org/10.3189/S0022143000023984>, 1958.
- Lienhard, J. H.: *A Heat Transfert Textbook*, pp. 411–428, Phlogiston Press, 2019.
- 390 Mangold, N.: Ice sublimation as a geomorphic process: A planetary perspective, *Geomorphology*, 126, 1–17, <https://doi.org/10.1016/j.geomorph.2010.11.009>, 2011.
- Mashaal, N. M., Sallam, E. S., and Khater, T. M.: Mushroom rock, inselberg, and butte desert landforms (Gebel Qatrani, Egypt): evidence of wind erosion, *International Journal of Earth Sciences*, 109, 1975–1976, <https://doi.org/10.1007/s00531-020-01883-z>, 2020.
- McIntyre, N. F.: Cryoconite hole thermodynamics, *Canadian Journal of Earth Sciences*, 21, 152–156, <https://doi.org/10.1139/e84-016>, 1984.
- 395 Michalski, J., Reynolds, S., Sharp, T., and Christensen, P.: Thermal infrared analysis of weathered granitic rock compositions in the Sacaton Mountains, Arizona: Implications for petrologic classifications from thermal infrared remote-sensing data, *Journal of Geophysical Research (Planets)*, 109, 3007–, <https://doi.org/10.1029/2003JE002197>, 2004.
- Mitchell, K. A. and Tiedje, T.: Growth and fluctuations of suncups on alpine snowpacks, *Journal of Geophysical Research*, 115, <https://doi.org/10.1029/2010JF001724>, number: F4, 2010.

- 400 Moeller, R., Moeller, M., Kukla, P. A., and Schneider, C.: Impact of supraglacial deposits of tephra from Grímsvötn volcano, Iceland, on glacier ablation, *Journal of Glaciology*, 62, 933–943, <https://doi.org/10.1017/jog.2016.82>, 2016.
- Nadeau, D. F., Brutsaert, W., Parlange, M., Bou-Zeid, E., Barrenetxea, G., Couach, O., Boldi, M.-O., Selker, J. S., and Vetterli, M.: Estimation of urban sensible heat flux using a dense wireless network of observations, *Environmental Fluid Mechanics*, 9, 635–653, <https://doi.org/10.1007/s10652-009-9150-7>, 2009.
- 405 Reid, T. D. and Brock, B. W.: An energy-balance model for debris-covered glaciers including heat conduction through the debris layer, *Journal of Glaciology*, 56, 903–916, <https://doi.org/10.3189/002214310794457218>, number: 199, 2010.
- Rhodes, J. J., Armstrong, R. L., and Warren, S. G.: Mode of Formation of “Ablation Hollows” Controlled by Dirt Content of Snow, *Journal of Glaciology*, 33, 135–139, <https://doi.org/10.3189/S0022143000008601>, 1987.
- Smiraglia, C. and Diolaiuti, G.: *Encyclopedia of Snow, Ice and Glaciers*, chap. Epiglacial Morphology, pp. 262–267, Springer, 2011.
- 410 Swithinbank, C.: The origin of dirt cones on glaciers, *Journal of Glaciology*, 1, 461–465, <https://doi.org/10.3189/S0022143000012880>, 1950.
- Taberlet, N. and Plihon, N.: Sublimation-driven morphogenesis of Zen stones on ice surfaces, *Proceedings of the National Academy of Sciences*, 118, <https://doi.org/10.1073/pnas.2109107118>, 2021.
- Turkington, A. V. and Paradise, T. R.: Sandstone weathering: a century of research and innovation, *Geomorphology*, 67, 229–253, <https://doi.org/10.1016/j.geomorph.2004.09.028>, 2005.
- 415 Vernay, M., Lafaysse, M., Monteiro, D., Hagenmuller, P., Nheili, R., Samacoits, R., Verfaillie, D., and Morin, S.: The S2M meteorological and snow cover reanalysis over the French mountainous areas, description and evaluation (1958–2020), preprint, *Cryosphere – Snow and Sea Ice*, <https://doi.org/10.5194/essd-2021-249>, 2021.
- Watson, R. D.: Spectral reflectance and photometric properties of selected rocks, *Remote Sensing of Environment*, 2, 95–100, [https://doi.org/https://doi.org/10.1016/0034-4257\(71\)90082-4](https://doi.org/https://doi.org/10.1016/0034-4257(71)90082-4), 1971.
- 420 Weady, S., Tong, J., Zidovska, A., and Ristroph, L.: Anomalous Convective Flows Carve Pinnacles and Scallops in Melting Ice, *Phys. Rev. Lett.*, 128, 044 502, <https://doi.org/10.1103/PhysRevLett.128.044502>, 2022.
- Young, R. and Young, A.: *Sandstone Landforms*, *Lecture Notes in Physics*, Springer-Verlag, <https://books.google.fr/books?id=Da8rvwEACAAJ>, 1992.
- Östrem, G.: Ice Melting under a Thin Layer of Moraine, and the Existence of Ice Cores in Moraine Ridges, *Geografiska Annaler*, 41, 425–228–230, <http://www.jstor.org/stable/4626805>, 1959.